Motor Neuron Morphology Estimation for its Classification in the Drosophila Brain

Gavriil Tsechpenakis, Ruwan Egoda Gamage, Michael D. Kim and Akira Chiba

Abstract— Type-specific dendritic arborization patterns dictate synaptic connectivity and are fundamental determinants of neuronal function. We exploit the morphological stereotypy and relative simplicity of the Drosophila nervous system to model the diverse dendritic morphologies of individual motor neurons (MNs) to understand underlying principles of synaptic connectivity in a motor circuit. The genetic tractability of Drosophila allows us to label single MNs with green fluorescent protein (GFP) and serially reconstruct identifiable MNs in 3D with confocal microscopy. Our computational approach aims at the robust segmentation of the MN volumes and the simultaneous partitioning into their compartments, namely the soma, axon and dendrites. We use the idea of co-segmentation, where every image along the z-axis (depth) is clustered using information from 'neighboring' depths. As appearance we use a 3D extension of Haar features and for the shape we define an implicit representation of the segmentation domain.

I. INTRODUCTION

Normal locomotive behavior is fundamentally determined by precise patterns of MN connectivity that are dictated by the selective connection of motor axons with muscle targets as well as specific dendritic input from presynaptic neurons. In the vertebrate spinal cord, MNs are organized into columns based on axonal projection patterns and within these columns, groups of MNs that target individual muscles are clustered into MN pools [7], [8]. Different MN pools elaborate distinct dendritic arborization patterns and respond to sensory stimulation with different latencies, demonstrating that the selectivity of synaptic input is directly influenced by the differential patterning of dendrites in the spinal cord [13].

Therefore, determining how different MN subtypes pattern and organize their dendrites in 3D space will be a crucial step toward understanding how motor circuits are assembled to control locomotion.

Drosophila larvae as a model. The Drosophila embryonic central nervous system (CNS) comprises the developing brain and ventral nerve cord (VNC) (**Fig. 1A**). The VNC, which can be considered functionally orthologous to the

G. Tsechpenakis and R. Egoda Gamage are with the Department of Computer and Information Science, Indiana University-Purdue University Indianapolis; gavriil@cs.iupui.edu, rjegodag@iupui.edu

M.D. Kim is with the Department of Molecular and Cellular Pharmacology, University of Miami Miller School of Medicine; mkim2@med.miami.edu

A. Chiba is with the Biology Department, University of Miami; akira.chiba@me.com
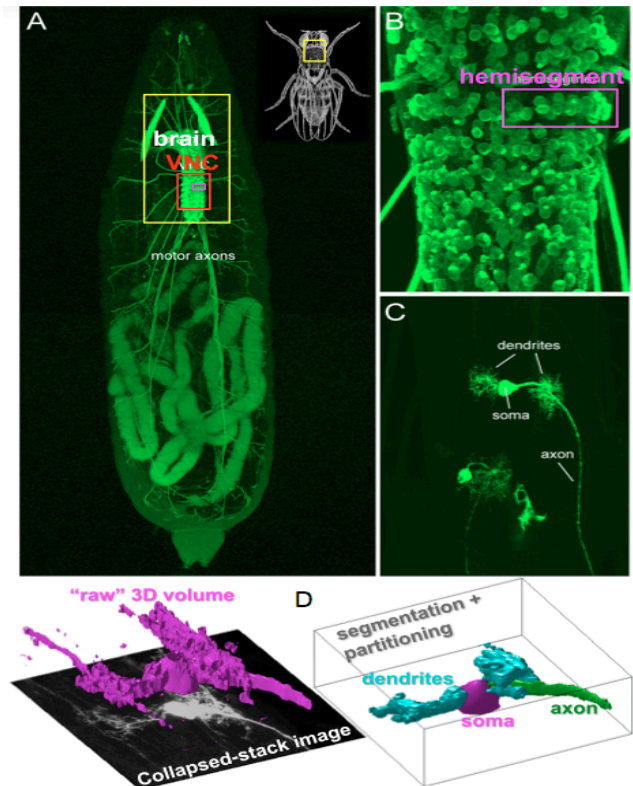
Fig. 1. **(A)** The whole larva with GFP expressed by the OK371-Gal4 driver [10] (all MNs shown); the panel also shows the CNS (brain and VNC) in relation to the whole animal. **(B)** Magnification of the VNC in the red box in (A); the magenta box illustrates a hemisegment. **(C)** Using MARCM we generate single MN clones which we analyze. **(D)** Single MN image stack depicts a noisy neuron volume; our goal is to segment the neuron from its surroundings and partition it in its compartments: soma, axon and dendrites.

mammalian spinal cord, is segmentally reiterated and bilaterally symmetrical with respect to the ventral midline. There are approximately 400 neurons, including an estimated 38 MNs, within each hemisegment (or half-segment) of the VNC (**Fig. 1B**). Abdominal hemisegments in the embryo comprise 30 stereotyped body wall muscles, each of which is innervated by one or more of the 38 MNs. The muscle innervation pattern of individual MNs is further highly stereotyped making embryonic MNs uniquely identifiable [6]. During larval development, dendrites of these abdominal MNs undergo considerable growth and dendritic branching is dramatically increased, likely reflecting extensive changes in synaptic connectivity that are required for more complex larval behaviors such as the peristaltic movements required for normal locomotion. Whether larval MNs project their dendrites to stereotyped regions of the VNC to create a connectivity map is unclear.
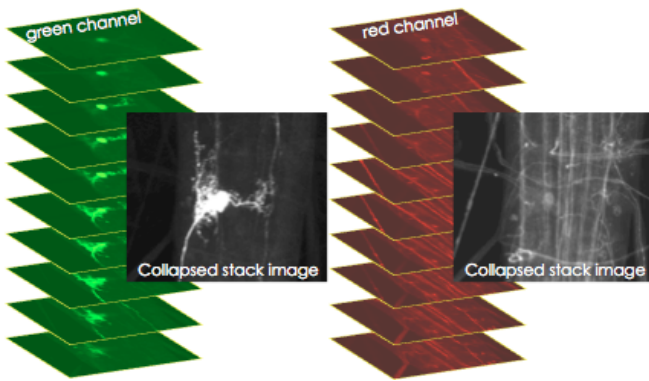
Fig. 2. Datasets for modeling individual neurons: the image stacks, one for each channel (green: neuron images; red: CNS reference images), with the grayscale images resulting from intensity summation along the z-axis.

II. IMAGING AT SINGLE-CELL RESOLUTION

Previous efforts to visualize morphology of single MNs have relied on dye-backfilling methods such as DiI. DiI is a lipophilic dye that is taken up by the axon and diffuses along the cell membrane to reveal neuronal morphology. However, this technique is limited in that neurons can only be labeled one at a time and dye-labeled neurons are more prone to photobleaching and phototoxicity. Furthermore, dye-labeling methods are not compatible with long-term sample preservation, limiting the use of secondary markers.

To overcome these limitations, we use mosaic analysis with a repressible cell marker (MARCM) [9], a genetic technique that allows us to label and image individual MNs (**Fig. 1C**). The use of fluorescent proteins allows for high-resolution in vivo imaging with minimal photobleaching, reduced phototoxicity and enhanced labeling of the neuronal membrane. Although labeled MNs generated by MARCM can be imaged live in the intact animal, muscle contraction by larva hinders the acquisition of confocal images through consecutive z positions. The brain and VNC are therefore exposed by dissection and the tissue is fixed with formaldehyde before immunostaining with antibodies directed against mCD8 (green channel) and a secondary marker, Fasciclin II (FasII) (red channel). FasII labels axon fascicles that divide the VNC into distinct territories and provides a frame of reference in which to map the relative positions of the MN soma and dendrites [5]. The entire morphology of single MNs is then imaged with laser scanning confocal microscopy that produces the image stacks to be analyzed (**Fig. 2**).

Our goal is to understand how connectivity patterns are formed within a normal motor circuit and to determine whether a 'connectivity map' can be deduced by estimations of neuronal morphology. Furthermore, developing a 3D model standard for different MN subtypes will allow for unbiased determinations of differences between neuronal morphologies in a wild-type and mutant brain. This will greatly facilitate our investigation into how different MN subtypes pattern their dendritic arbor to establish synaptic connectivity, which remains an understudied yet important aspect of motor circuit formation. Lastly, understanding the normal process of MN development will ultimately be
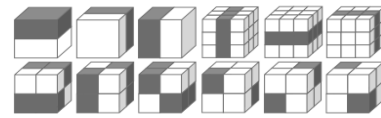

Fig. 3. Examples of the Haar masks in the 3D domain: $\{gray = -1, white = +1\}$.

important in devising strategies to repair or restore MN connectivity after spinal cord injury or disease.

III. NEURON MORPHOLOGY ESTIMATION

The neuron volume does not provide the necessary information for the desired morphology-based MN classification. According to the study in [4], the morphological features that uniquely describe individual MN subtypes are the relative positions between soma, axon, and dendrites, along with the shapes and extends in the 3D space of these compartments. To calculate such features we need to partition the neuron volume into these three morphologically distinct subvolumes. From **Figs. 1, 2** it is apparent that while intensity determines the neuron volume, shape is what describes the compartment label: soma is an ellipsoid, axon is an elongated structure and dendrites have an arbitrary shape. However, high variability in morphology, even for MNs of the same subtype, does not allow for partitioning using existing shape-constrained models, e.g., Active Shape Models [1].

Our approach is based on the principle of co-segmentation, mainly used for simultaneous segmentation of a collection of images [3], [2]. It exploits the idea of sharing knowledge for the targets appearance throughout the input set, instead of using training samples. Here the collection of images is the image stack. We use co-segmentation to partition each image into soma, axon and dendrites, and estimate the 3D morphology from the 2D results. We over-segment all images and we merge the resulting regions using shape and appearance. To obtain more robust intensity information, we use Haar-like features [12] in a 3D manner as shown in **Fig. 3**, with fixed mask size. In our experiments, and for $1024 \times 1024 \times 30$ dataset size, we used $25 \times 25 \times 5$ Haar masks.

We assume intensity continuity/smoothness along the z-axis. If a region of interest exists at a given depth, then part of it should also exist at neighboring depths. We use this as a soft constraint to account for progressively appearing/disappearing regions over depth, which depicts the arbitrary 3D shapes of the neuron compartments. We also assume that the neuron soma is (partially) visible in the first image of the stack to facilitate the shape description below.

A. Shape representation

We define a representation of 2D shape sets using distance functions [11], which incorporates information about the relative positions of the neuron compartments. Let Ω be the (2D) image domain and $\mathcal{C} = \{C^k\}_{k=1}^{K}$ is the result of an intensity-based over-segmentation of Ω, where C^k is the k-th segment and K is the total number of segments. For calculating $\mathcal{C}$ we use the K-means algorithm, although other methods (e.g., watershed and graph-cuts) can also be used.
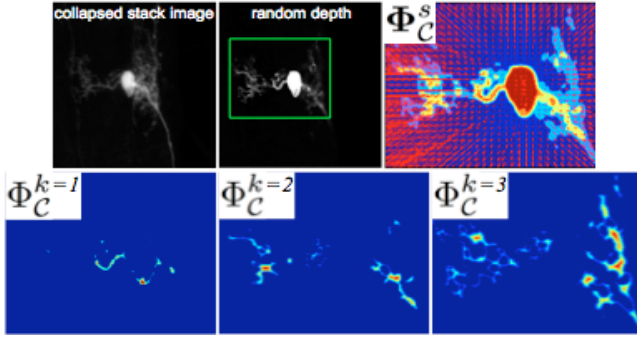
Fig. 4. Shape representation of a random segmentation set $\mathcal{C}$. First row (from left to right): collapsed stack image; image at a random depth; an over-segmentation set $\mathcal{C}$, with the reference segment C^s in red and its directed distance (vector field) $\Phi_{\mathcal{C}}^s$ superimposed. Second row: the distance functions $\Phi_{\mathcal{C}}^k$ for every segment $C^k \neq C^s$.

We consider the soma region, the least variable structure, as the ***reference segment***. Soma regions exist in the first images of the stacks. Let $C^s \subset \mathcal{C}$ denote the soma segment. If soma is over-segmented and/or there are regions from other compartments present at the given depth, then C^s is chosen as the segment without holes and whose boundary best fits a circle. The directed (vector) distance function $\Phi_{\mathcal{C}}^s$ of the reference segment describes its shape but also the relative positions of all other segments $\{C^k\}_{k=1,k \neq s}^K$,

$$\Phi_{\mathcal{C}}^s = \mathbf{d}(\mathbf{x}, \mathcal{B}^s), \forall \mathbf{x} \in \Omega \qquad (1)$$

where $\mathbf{d}(\mathbf{x}, \mathcal{B}^s)$ is the vector distance of every $\mathbf{x} \in \Omega$ from the reference segment boundary $\mathcal{B}^s$. The magnitude and direction of $\Phi_{\mathcal{C}}^s$ represent the relative position of every $\mathbf{x} \in \Omega$ and therefore of every segment (**Fig. 4**). Also, the shape of each segment C^k, $k \neq s$, is described with a distance function $\Phi_{\mathcal{C}}^k$ independently from the set $\mathcal{C} \backslash C^k$,

$$\Phi_{\mathcal{C}}^k = \begin{cases} d(\mathbf{x}, \mathcal{B}^k), \forall \mathbf{x} \in C^k, k \neq s \\ 0, \; otherwise \end{cases}, \qquad (2)$$

where $d(\mathbf{x}, \mathcal{B}^k)$ is the distance of every $\mathbf{x} \in C^k$ from the segment boundary $\mathcal{B}^k$ (**Fig. 4**). Then, the neuron region at a specific depth, given a segmentation outcome $\mathcal{C}$, can be defined as a vector field,

$$\Phi_{\mathcal{C}} = \left[\Phi_{\mathcal{C}}^s, \sum_{k=1,k \neq s}^K \Phi_{\mathcal{C}}^k \right], \qquad (3)$$

given that $C^i \cap C^j = \emptyset$, $i \neq j$, i.e., for a given $\mathbf{x} \in \Omega$, $\Phi_{\mathcal{C}}^i(\mathbf{x})$ and $\Phi_{\mathcal{C}}^j(\mathbf{x})$ cannot both have non-zero values.

B. Co-segmentation

Let $\mathcal{I}^{(z)}$ be an image in the stack at depth z, and H be the total number of Haar features [12] (**Fig. 3**) estimated from the images $\mathcal{I}^{(z \pm \delta z)}$, $\delta z = 1, \ldots, (m-1)/2$, with m being the z-dimension of each Haar mask. We calculate H over-segmentation sets $\mathcal{C}_h^{(z)}$, one for each feature (left panel of **Fig. 5**). Our goal is to combine the results of all H features from the m depths around z to obtain the final segmentation $\tilde{\mathcal{C}}^{(z)}$ for $\mathcal{I}^{(z)}$. $\tilde{\mathcal{C}}^{(z)}$ must contain segments of only three classes (soma, axon and dendrites); the first two have distinctive shapes as we describe above. Therefore, co-segmentation is driven by shape as defined in eqs. (1)-(3). The objective is the loss function to be minimized,

$$\mathcal{E} = \epsilon_c + \epsilon_{\delta z} + \epsilon_s, \qquad (4)$$

where the three penalty terms are defined as follows.

(a) The inconsistencies over the set $\{\mathcal{C}_h^{(z)}\}_{h=1}^H$, i.e., *disagreement* $\Delta^k(i,j)$ between the outcomes of all pairs i, j of features for all segments k,

$$\epsilon_c = \sum_{k=1}^K \left[\sum_{(i,j)=1,i \neq j}^H \Delta^k(i,j) \right], \qquad (5)$$

where $\Delta^k(i,j) = \int_\Omega \left[C_i^{k,(z)} \cup C_j^{k,(z)} - C_i^{k,(z)} \cap C_j^{k,(z)} \right](\mathbf{x}) d\mathbf{x}$ for a given k, and $C_i^{k,(z)}$ is the k-th segment of the i-th segmentation set at depth z.

(b) If $\Phi_h^{(z)}$ is the shape of the segmentation outcome $\mathcal{C}_h^{(z)}$, for the h feature at depth z, we penalize shape variations for each feature h over neighboring depths,

$$\epsilon_{\delta z} = \sum_{h=1}^H \left[\sum_{(i,j)=z-\delta z, i \neq j}^{z+\delta z} \left[\Phi_h^{(i)} - \Phi_h^{(j)} \right] \right], \qquad (6)$$

(c) For each segment k, let $\mathcal{M}^k$ be an $H \times H$ structure (hypermatrix), where $\mathcal{M}^k(i,j)$ is the shape histogram of $C_i^{k,(z)} \cup C_j^{k,(z)}$, calculated using the non-negative areas of the distance functions in eq. (2) [11]. Let q_c and q_e be the normalized shape histograms of an *average* soma (circle-like) and axon (elongated structure), estimated manually from existing datasets. The Bhattacharyya distances $D[\mathcal{M}^k(i,j), q_c]$, $D[\mathcal{M}^k(i,j), q_e]$ indicate shape similarity of $\mathcal{M}^k(i,j)$ with the two shape priors [11]. We penalize shape dissimilarities from the target shapes as,

$$\epsilon_s = \sum_{k=1}^K \sum_{(i,j)=1,i \neq j}^H D[\mathcal{M}^k(i,j), q_c] D[\mathcal{M}^k(i,j), q_e], \qquad (7)$$

The method in steps. Given an image stack $\{\mathcal{I}^{(z)}\}_{z=1}^Z$:
(i) For every $\mathcal{I}^{(z)}$ obtain initial segments $\mathcal{C}_h^{(z)}$ for each Haar feature h separately.
(ii) Locate the reference segment (soma) by calculating the union of all reference segments in the sets $\mathcal{C}_h^{(z)}$.
(iii) Calculate the shapes $\Phi_h^{(z)}$.
(iv) Calculate the cost terms ϵ_c, ϵ_s.
(v) Calculate the cost $\epsilon_{\delta z}$ considering neighboring depths $[z - \delta z, z + \delta z]$ (repeat (i)-(iii) for $z \pm \delta z$ in the first iteration only).
(vi) Calculate $\mathcal{E}$.
(vii) Merge segments from the sets $\mathcal{C}_h^{(z)}$ that yield lower values of $\sum_{(i,j)=1,i \neq j}^H D[\mathcal{M}^k(i,j), q_c] D[\mathcal{M}^k(i,j), q_e]$.
(viii) Update sets $\mathcal{C}_h^{(z)}$ and repeat (iii) - (vii).
(ix) Repeat (i)-(viii) for $\mathcal{I}^{z+1}$.

The right panel in **Fig. 5** illustrates the result of steps (i)-(viii) for an image at a given depth.

Finally, to obtain the 3D morphology of the neuron, by combining the segmentation results across all depths in the given stack, we adopt the Delaunay-based surface reconstruction method in [14].

IV. RESULTS

Our MARCM experiments and imaging studies have thus far yielded over 150 high-resolution image stacks of 28
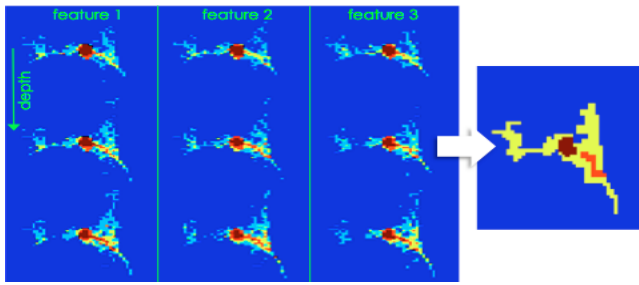
Fig. 5. Co-clustering using three Haar features over three successive images in the stack. Left: individual over-clustered features. Right: co-segmentation result.
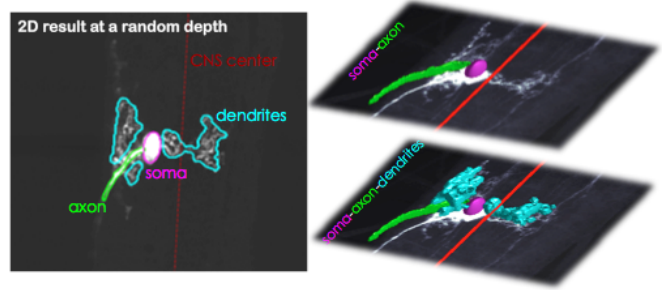

Fig. 6. Indicative segmentation results for a given dataset. Left: segmentation of a random image in the stack; the CNS center is also illustrated with a dashed red line. Right: 3D results using our co-segmentation with the method in [14].
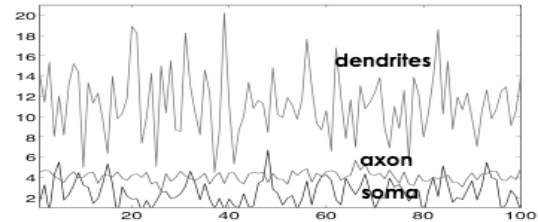

Fig. 7. Solution stability for different segment over-segmentation initializations: the average segmentation errors calculated from eq. (8) for each neuron compartment separately. The x-axis corresponds to repetitions of the k-means algorithm that produce different segments as initialization for our method.

unique larval MN subtypes [4]. We analyzed 35 randomly chosen datasets depicting 4 MN subtypes (MN1,9,15,16). In all datasets, the estimated and manually labeled compartment subvolumes largely coincide, which is sufficient for the desired morphology-based MN recognition, as shown in **Fig. 6**: the estimated relative positions between the compartments coincide with the findings in [4].

However, we validate the accuracy of our method and define as error the percentage (%) of misclassified pixels with respect to the compartment area (2D) and volume (3D),

$$error = \frac{|ground\ truth - estimated|}{ground\ truth} \qquad (8)$$

Here we report *[average, worst-case]* classification errors from two comparison approaches.

(i) We manually traced soma, axon and dendrites boundaries for each image in a given stack and compared the resulting areas with our partitioning results: soma $\Rightarrow$ [2.3, 6.8]; axon $\Rightarrow$ [4.1, 5.7]; dendrites $\Rightarrow$ [11.3, 20.4].

(ii) We interpolated the manually traced boundaries over depth, calculated the 3D volume, and compared it with our estimated volume after the 3D reconstruction: soma $\Rightarrow$ [5.1, 7.9]; axon $\Rightarrow$ [6.3, 7.2]; dendrites $\Rightarrow$ [10.8, 18.7].

As anticipated, the segmentation of the soma yields lower errors, due to the relatively homogeneous intensity, its smooth variation over depth, and the small shape variation. Also, the intensity inhomogeneities and random shapes of the dendrites make their accurate segmentation more challenging. The higher errors we report for the estimation of the volumes are mainly due to the fact that we applied the 3D reconstruction without data-driven constraints across different depths. This is an issue that we will tackle in our future work.

Finally, we validated the stability of our solution for different initializations; the plot in **Fig. 7** shows the segmentation errors for the three compartments over 100 different initial over-segmentations with k-means.

V. CONCLUSIONS AND FUTURE DIRECTIONS

The morphological properties of a neuron have a direct influence on patterns of synaptic connectivity. We developed a method for the reconstruction of the neuron morphology, in order to create 3D models standard for different MN subtypes in the Drosophila nervous system. Such models will serve as a predictive tool for the assembly of motor circuits in the normal and mutant brain. Our future work includes the extension of our co-segmentation framework in 3D with the introduction of local 3D shape and appearance smoothness constraints.

REFERENCES

[1] T.F. Cootes, C.J. Taylor, D.H. Cooper, and J. Graham, Active shape models - their training and application, *Computer Vision and Image Understanding*, 61(1): 38-59, 1995.
[2] D.S. Hochbaum and V. Singh, 'An efficient algorithm for co-segmentation,' *ICCV*, 2009.
[3] A. Joulin, F. Bach, and J. Ponce, 'Discriminative Clustering for Image Co-segmentation,' *CVPR*, 2010.
[4] M.D. Kim, Y. Wen, and Y.N. Jan, 'Patterning and organization of motor neuron dendrites in the Drosophila larva,' *Dev Biol.*, 336: 213-221, 2009.
[5] M. Landgraf, N. Sanchez-Soriano, G.M. Technau, J. Urban, and A. Prokop, 'Charting the Drosophila neuropile: a strategy for the standardised characterisation of genetically amenable neurites,' *Dev Biol.*, 260: 207-225, 2003.
[6] M. Landgraf, T. Bossing, G.M. Technau, and M. Bate, 'The origin, location, and projections of the embryonic abdominal motorneurons of Drosophila,' *J. Neurosci.*, 17: 9642-9655, 1997.
[7] L. Landmesser, 'The distribution of motoneurones supplying chick hind limb muscles,' *J. Physiol.*, 284: 371-389, 1978.
[8] L. Landmesser, 'The development of motor projection patterns in the chick hind limb,' *J. Physiol.*, 284: 391-414, 1978.
[9] T. Lee and L. Luo, 'Mosaic analysis with a repressible cell marker for studies of gene function in neuronal morphogenesis,' *Neuron*, 22: 451-461, 1999.
[10] Mahr and H. Aberle, 'The expression pattern of the Drosophila vesicular glutamate transporter: a marker protein for motoneurons and glutamatergic centers in the brain,' *Gene Expr Pat.*, 6: 299-309, 2006.
[11] G. Tsechpenakis and D. Metaxas, 1CoCRF Deformable Model: A Geometric Model Driven by Collaborative Conditional Random Fields,' *IEEE Trans. Image Processing*, 18(10): 2316-2329, 2009.
[12] P. Viola and M. Jones, 'Rapid object detection using boosted cascade of simple features,' *CVPR*, 2001.
[13] E. Vrieseling and S. Arber, 'Target-induced transcriptional control of dendritic patterning and connectivity in motor neurons by the ETS gene Pea3,' *Cell*, 127: 1439-1452, 2006.
[14] D. Wang, O. Hassan, K. Morgan, and N. Weatherill, 'Efficient surface reconstruction from contours based on two-dimensional Delaunay triangulation, *Int'l Journal for Numerical Methods in Engineering*, 65(5): 734-751, 2006.